VIRTUAL AND PHYSICAL PROTOTYPING
2025, VOL. 20, NO. 1, e2499925 (18 pages)
https://doi.org/10.1080/17452759.2025.2499925

Taylor & Francis
Taylor & Francis Group

Generative adversarial network–enabled microstructural mapping from surface profiles for laser powder bed fusion

Jingwen Gao[a,b], Chenyang Zhu[a], Shubo Gao[a], Weiming Ji[a], Ming Xue[b] and Kun Zhou[a]

[a]Singapore Centre for 3D Printing, School of Mechanical and Aerospace Engineering, Nanyang Technological University, Singapore; [b]Infineon Technologies Asia Pacific Pte. Ltd., Singapore

ABSTRACT
Laser powder bed fusion (LPBF) is the dominant metal additive manufacturing technique due to its advantages in near-net-shape production of complex parts with high resolution. However, conventional quality control of LPBF-fabricated parts, including microstructure characterisation, often relies on trial-and-error experiments. These methods can be time-consuming, resource-intensive, and potentially destructive to specimens. This study introduces an image-to-image translation Cycle-consistent Generative Adversarial Network (CycleGAN)-based framework for generating statistically equivalent microstructures of LPBF-fabricated samples directly from corresponding as-printed surface inputs. The results demonstrate that the framework can effectively generate crystallographic and morphological features across 22 different process parameters for LPBF-fabricated pure nickel. The distribution of microstructural descriptors, such as grain size, grain shape, and even grain boundary misorientation angles, shows no significant difference from that measured by experiments. The generated microstructural mapping using image inputs with CycleGAN outperforms those from other generation methods on both qualitative and quantitative evaluations. The developed framework is material-agnostic and can be fine-tuned for other LPBF materials via transfer learning, providing potential applications in in-situ process optimisation and microstructure design in LPBF manufacturing.

ARTICLE HISTORY
Received 23 December 2024
Accepted 8 April 2025

KEYWORDS
Microstructure; surface morphology; generative adversarial network; laser powder bed fusion

1. Introduction

Laser powder bed fusion (LPBF) is a dominant additive manufacturing technique that fabricates intricate components by selectively melting layers of metal powder with a high-powered laser [1–4]. The unique solidification path with extremely high cooling rate, and intrinsic multiple thermal cycles in LPBF result in special microstructure compared to conventional manufacturing. The properties of LPBF-fabricated components, such as strength and ductility, heavily depend on microstructural features such as grain size, texture, phase distribution, and defects [5–7], which are influenced by a complex interplay of multiple process parameters, including laser power, scan speed, and layer thickness [8–10]. Precise calibration of these parameters is crucial for optimising microstructures and achieving desired properties.

The traditional approach for understanding the process – microstructure (PM) relationship in LPBF-fabricated materials has relied on trial-and-error experiments, where various processing conditions are systematically tested to observe their impact on microstructures. Metallography, the study of metal microstructures, typically employs techniques like optical microscopy (OM), scanning electron microscopy (SEM), and electron backscatter diffraction (EBSD) to reveal the microstructural features. While these methods provide valuable insights into a material's history and properties, they are often time-consuming, resource-intensive, and destructive – limitations that are particularly problematic for geometrically complex components produced using LPBF [11].

To complement the experimental method, microstructure simulations, especially physics-based models such as cellular automata [12] and phase-field [13] simulations, have been developed based on established governing laws to predict the microstructures from given process conditions. While these models successfully simulate microstructure evolution, many require simplifications [14–16], such as assuming spherical powder particles, a constant thermal gradient, and a point

CONTACT Kun Zhou kzhou@ntu.edu.sg Singapore Centre for 3D Printing, School of Mechanical and Aerospace Engineering, Nanyang Technological University, Singapore 639798

Supplemental data for this article can be accessed online at https://doi.org/10.1080/17452759.2025.2499925.

heating source, to make the computations feasible. These simplifications can overlook critical variables and interactions related to the model and process parameters [17], potentially compromising the accuracy and reliability of predictions in real-world scenarios. On the other hand, more detailed and accurate models often demand substantial computational resources, making them impractical for large-scale applications.

Based on the disadvantages of traditional metallurgical and simulation methods, developing a non-destructive method to quickly visualise microstructure of LPBF parts can effectively enhance our understanding of the PM relationship. Image-based machine learning (ML) techniques have been instrumental in this area, leveraging data from OM, SEM, and EBSD images to uncover previously hidden patterns in the complex PM relationship. Examples include microstructure image generation, grain segmentation and inference, EBSD image super-resolution, density prediction, and surface-internal defect correlation analysis [18–27]. For microstructure image generation, current research predominantly focuses on phase distribution, often neglecting critical details related to crystallographic orientations and grain morphology, which play a significant role in determining the properties of LPBF fabricated samples. Additionally, existing studies typically investigate a limited set of process parameters, which may not capture the complex interactions among multiple variables that collectively influence microstructure formation. As a result, the chosen parameters might not fully represent the wide array of microstructural phenomena that occur under different processing conditions.

Among popular generative algorithms, Generative Adversarial Networks (GANs) [28] have become the cutting-edge approach in microstructure image generation. The adversarial training process enables GANs to produce highly authentic images across various domains, including LPBF. Conditional GANs (CGANs) [29] and Cycle-consistent GANs (CycleGANs) [30] are two variations of popular GANs developed to handle text and image inputs, respectively. In microstructure image generation, CGANs have been more frequently used. For instance, Cao et al. [18] and Banko et al. [31] employed CGANs to generate micrographs conditioned on specific processing parameters, such as deposition temperature, laser power, and material compositions. CycleGANs are usually applied for microstructure image translation [32,33]. They are unsupervised models that do not require paired datasets. They learn feature relationships between the input domain and the target domain [34] with two generator-discriminator pairs [35]. In this surface-to-microstructure mapping, where the input is an image and obtaining paired datasets is challenging, CycleGAN stands out as a more suitable option than other GAN models due to its ability to learn from unpaired data while maintaining the fidelity of the structural details during the translation process. It generates new images that reflect the characteristics of the microstructure domain based on the surface image's structure and content. The diverse microstructural maps generated can be particularly useful for data augmentation in material data mining [36].

In this study, a CycleGAN-based framework was developed to generate statistically equivalent microstructures of LPBF-fabricated nickel directly from corresponding as-printed surface inputs across various process parameters. The model was trained on an experimentally collected dataset from LPBF samples subjected to various combinations of laser power, scan speed, and hatch spacing. These surface profiles directly reflect the processing conditions and correlate with the thermal history during the building process. The proposed model aims to reveal the complex correlations between surface profiles and the crystallographic characteristics of the fabricated specimens. The generated microstructure mapping captures key morphological and crystallographic features, including grain sizes and shapes, crystallographic texture, and defects. The trained model can synthesise microstructure mappings across a wide LPBF parameter window in negligible time as compared to the effort for experimental data collection. It can also be readily extended to other LPBF materials via transfer learning, requiring minimal additional training. The inferred microstructures can benefit both academia, by providing a multitude of reliable microstructure mappings for simulation work, and industrial settings, by optimising parameters and enabling inline quality evaluation and control of the LPBF process.

2. Methods

2.1. Sample preparation

Pure nickel (purity 99.5 wt%) powder exhibiting particle diameter in a range of 15–53 µm was used for LPBF process. It was selected as the raw material to print the samples and collect experimental data for training and evaluating the models due to the high printability of most FCC alloys and its wide usage in the industry [37]. As a common test material for crystallographic measurement [38,39], the simplicity of nickel's microstructure allows the models to easily identify the features from limited training data and focus on fundamental relationships without being overwhelmed

Table 1. Processing variables applied in the experiments.

	Sample number	Laser power (W)	Hatch spacing (mm)	Scan Speed (mm/s)	Sample number	Laser power (W)	Hatch spacing (mm)	Scan Speed (mm/s)
Train	1	100	0.08	600	9	200	0.08	1000
	2	120	0.08	600	10	200	0.08	700
	3	140	0.08	600	11	200	0.08	800
	4	160	0.08	600	12	200	0.08	900
	5	180	0.08	600	13	200	0.06	600
	6	200	0.08	600	14	200	0.04	600
	7	200	0.08	400	15	200	0.1	600
	8	200	0.08	500	16	200	0.12	600
Test	17	160	0.07	400	20	100	0.12	1000
	18	190	0.1	550	21	120	0.04	950
	19	180	0.06	650	22	100	0.04	900

by unnecessary complexity. Its well-characterised microstructure in EBSD studies also provide a reliable and standardised basis for transfer learning to other materials and comparative analysis.

Table 1 enlists the combinations of laser power (*P*), scan speed (*v*), and hatch spacing (*h*) used for 16 training samples and 6 testing samples. The choice of value ranges for the three changing process parameters was based upon established process window [40]. The main objective was to comprehensively cover different surface morphologies, levels of porosity, and microstructural features, for LPBF-fabricated Ni samples. Apart from the varying parameters, a fixed layer thickness (*t*) of 0.03 mm and a bidirectional scanning strategy (Figure 1(a)) with a rotation of 90° in the fabrication of each subsequent layer were implemented [37]. The final build dimension of each cubic sample was $6 \times 6 \times 6$ mm^3. All samples were printed using a customised LPBF machine, equipped with a 200 W IPG fibre laser source of 1070 nm wavelength. The laser beam diameter was 100 µm, and all fabrications were carried out in nitrogen atmosphere with oxygen concentration below 1000 ppm to minimise oxidation.

The surface and microstructure used in this study refer to the top surface and internal microstructure, respectively, as shown in Figure 1(b). The top surfaces of all printed cubes were characterised by three different microscopes. The optical micrograph was captured using optical microscope (OM, Olympus LEXT OLS4100). Surface height profile was measured using laser scanning confocal microscope (LSCM, Keyence VK-X series) with a magnification of ×20 and a z-depth resolution of 2 µm in high-speed mode. To enhance surface feature contrast and improve model's feature extraction efficiency, the surface height profile was normalised across all samples. A finer characterisation of the surface was achieved by scanning electron microscope (SEM, JOEL JSM-7800F Prime). The acquired images of the surface are in size of 6×6 mm^2. An alignment and centre crop were performed on these surface images to obtain identical region of interest and eliminate the edge effect [41]. The internal microstructure is characterised by EBSD using the same SEM equipped with EBSD detector (Oxford Instrument, Symmetry). EBSD was conducted using a step size of 1 µm and covering an area of 0.5×0.5 mm^2 on the perpendicular cross-section from

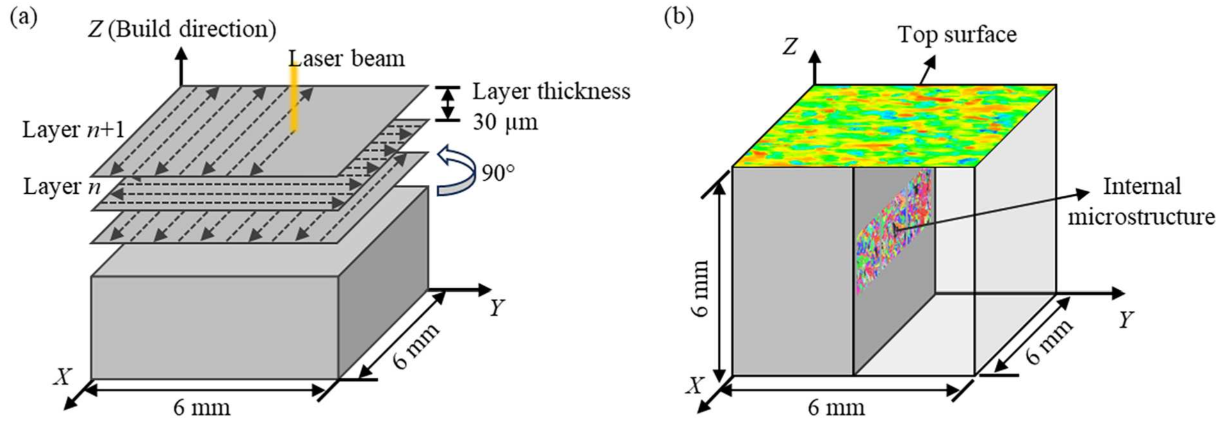

Figure 1. (a) Schematic of the scan strategy of a $6 \times 6 \times 6$ mm^3 part fabricated by the LPBF and (b) illustration of the locations where the surface profiles and microstructure maps were acquired.

Table 2. Types of images and their corresponding preprocessing configurations.

Image types		Image size (pixels)	Measured size (mm^2)	Patch size (pixels)
Surface	Optical	1161 × 1161	5.0 × 5.0	387 × 387
	SEM	2730 × 2730		910 × 910
	Height	650 × 650		256 × 256
Microstructure	EBSD	1614 × 1614	0.5 × 0.5	635 × 635

the approximate centre region of the printed samples. Such region experiences a relatively more stable thermal history, being more representative of LPBF processing conditions and minimising the boundary effect in microstructures [42]. The perpendicular plane was selected as it effectively captures the layer-by-layer build structure characteristics of the LPBF process and is particularly informative for analysing microstructural features.

2.2. Image data handling

The original data resolution for surface and microstructure images are listed in Table 2. These high-resolution images contain characteristic features that repeat across the entire image. To obtain a dataset with an adequate number of training images and maintain computational efficiency, patches were extracted at random points of each image. This approach also ensures that the model remains applicable to LPBF-fabricated Ni samples with varying dimensions, as the extracted patches can consistently represent equivalent areas of interest with uniform image resolution, regardless of the sample size [43]. The patch sizes for surface and microstructure are included in Table 2. Since the surface feature sizes range from few micrometres to more than 1 ml, and the largest hatch spacing is 0.12 mm, the patch size values were chosen to cover 40% in length and width of the original data. This ensures that each extracted patch covers a sufficiently large area to represent characteristic features, such as defects arising from the synthesis conditions. Additionally, since the patches are randomly cropped, there will be overlap between them, ensuring that critical features near patch boundaries are not missed. A total of 256 patches were cropped per sample, resulting in a dataset of 4096 images for each image type. This dataset is split randomly at a ratio of 75:25 to form the training and validation datasets.

3. GAN models

3.1. Model architecture

In this study, CGAN and CycleGAN architectures were employed to handle process parameter inputs and surface profile inputs, respectively. The quality of generated images and their accuracy in representing the real microstructure were subsequently compared. Both architectures were implemented in Python using Keras library with a TensorFlow backend. The training and testing were conducted on one NVIDIA Tesla A100 40GB GPU.

The CycleGAN model's architecture employed in this study is illustrated in Figure 2. It consists of two U-Net based generators (G and F) and two convolutional 70 × 70 PatchGAN discriminators (D_x and D_y). The training dataset of CycleGAN comprises both surface profiles and orientation maps, each with a size of 256 × 256 × 3. All these images were normalised to the $[-1, 1]$ range before being input into the model to stabilise and speed up the computations. The generators have an encoder–decoder structure with skip connections. The encoder consists of convolutional layers with stride-2 convolutions, each followed by instance normalisation and LeakyReLU activation function. This process reduces the input surface image's spatial dimensions to 1 × 1 × 512 using eight downsampling blocks. The decoder uses transposed convolutional layers to upsample the features back to their original image size, with each layer followed by instance normalisation and ReLU activation function. The discriminators receive both real and generated image patches to assess their realism. Instead of producing a single scalar output, the discriminators output a matrix where each element represents the probability that the corresponding image patch is real. This patch-based approach enables the discriminator to capture finer details and textures. In addition to the adversarial losses, cycle consistency losses are introduced to measure the L1 norm (absolute difference) between the reconstructed images and the originals. These losses diligently retain the integrity of the transformed images by necessitating that the reverse transformations return the generated images back to their original domain. This compelling enforcement allows the model to generate images that uphold the physical and morphological attributes consistent with the target microstructures. The full loss function is:

$$\begin{aligned} L(G, F, D_x, D_y) = {} & L_{\text{GAN}}(G, D_y, X, Y) \\ & + L_{\text{GAN}}(F, D_y, X, Y) \\ & + \lambda L_{\text{cyc}}(G, F), \end{aligned} \tag{1}$$

where X and Y are the source and target domains, respectively, and $\lambda = 10$ controls the relative importance of the two objectives. The entire network was trained for 20 epochs, using the Adam optimiser with learning rate of 0.0002 and beta_1 of 0.5. Besides,

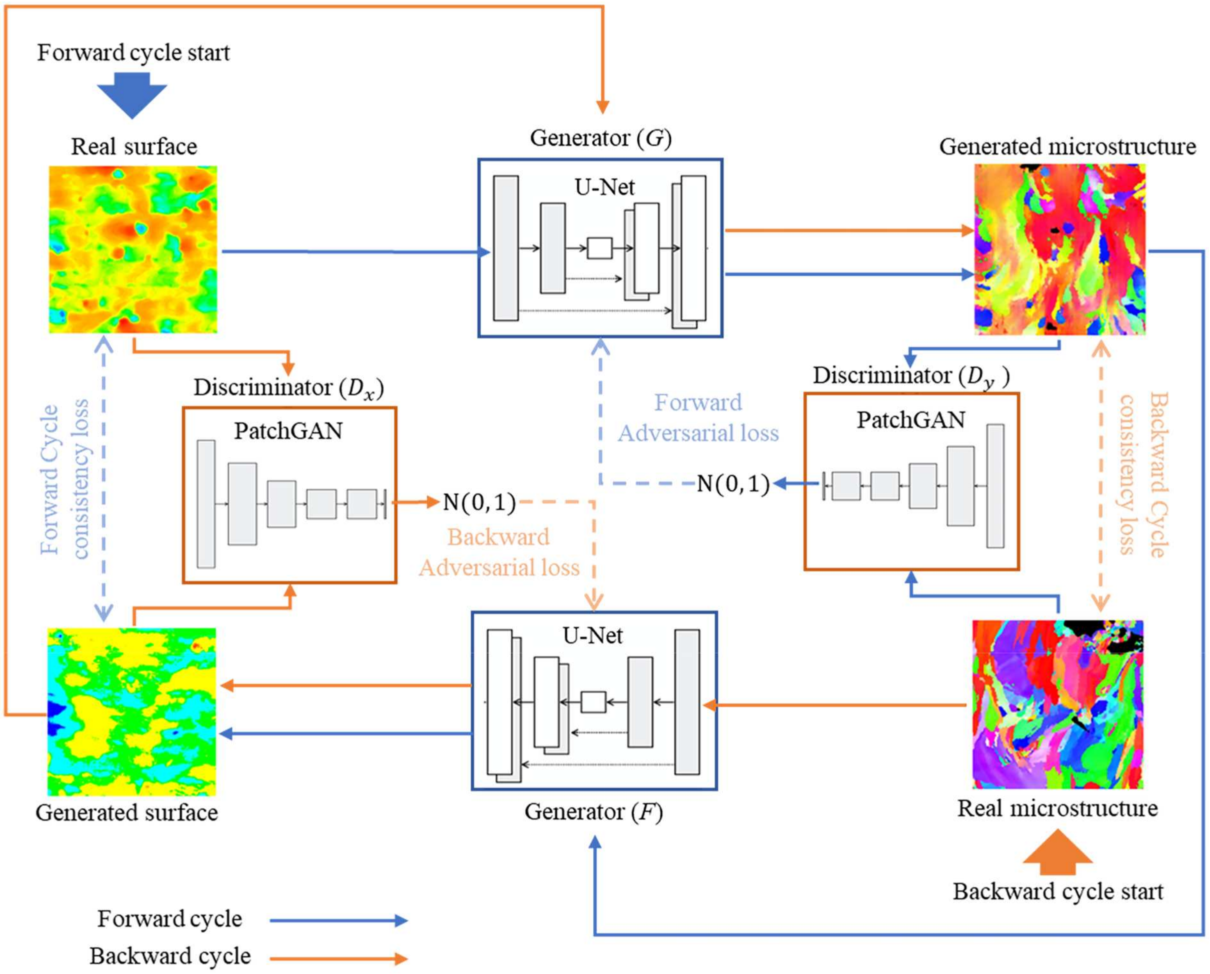

Figure 2. Framework of the CycleGAN model used for the microstructure reconstruction and prediction.

weights were initialised using a Gaussian distribution to promote effective training convergence.

The CycleGAN used surface profiles–height maps measured by a laser confocal microscope as inputs. These surface profiles offer a more objective representation of the processing conditions, capturing material-related information with minimal human intervention. The model was trained to generate microstructural maps, specifically orientation maps measured by EBSD. Each pixel on the output map contains Euler angle triplets representing the information of its corresponding crystal orientation. For clarity and consistency with EBSD inverse pole figure (IPF) maps, all the generated maps were coloured using the IPF colour code, illustrating the local crystal orientation. The LPBF-fabricated microstructures exhibit distinctive microstructural features, including grain shape, size, and orientation. These characteristics manifest as unique spatial patterns in the EBSD IPF map. The convolutional calculations performed by kernels in each layer of the U-Net generators effectively extract relevant style and structural information from the original data [44]. The PatchGAN discriminators [45] receive fake patches from the generators' predictions and compare the patches with real microstructure patches. During iterative training, the discriminators learn to assign high probabilities to real patches and low probabilities to fake patches, providing feedback to the generators which helps to adjust their trainable weights continually through backpropagation. The learned weights in the neural networks encode essential features such as colour distribution, object shapes, and edges about the training data, facilitating accurate microstructure reconstruction.

Most existing studies on material microstructure generation use CGAN models conditioned on text-based parameter inputs [29]. These studies have shown that CGAN can successfully map between the process parameters and microstructural features such as phase morphology and particle size [18,19]. In this work, CGAN is trained to generate microstructure maps directly from the process parameter combinations and serves as a benchmark for the model performance comparison with the CycleGAN.

The CGAN model's architecture is illustrated in Supplementary Figure 1. The model was trained for 100 epochs with a batch size of 8. Adam optimiser with a learning rate equal to 0.0002 and beta_1 equal to 0.5 was used for both generator and discriminator. The generator takes two inputs: a 32-dimensional latent vector and 3 printing parameters (i.e. laser power, scan speed, and hatch spacing), which were concatenated after being reshaped to 16×16 metrices and passed into convolutional-transpose layers for upscaling. These metrices were upscaled with a stride size of 2 and 128 filters followed by Leaky ReLU activation function. The final convolutional layer used hyperbolic tangent activation function and output an image with a size of $64 \times 64 \times 3$. This smaller output image size was experimentally determined and used for the CGAN to improve the perceived quality of the generated images and prevent overfitting. The model struggles with higher resolutions due to the limited data available. The discriminator has a similar but inverted structure. It also takes two inputs: an image, either real or generated, and the same 3 printing parameters. In this adversarial network training, the discriminator uses a binary cross-entropy loss function, while the generator loss is calculated from the discriminator's misclassification.

3.2. Post-processing of generated mapping

The generated Euler angle map was transformed into an IPF colour-coded map using the MTEX package in MATLAB [46]. Grain boundary regions were identified through MATLAB's built-in edge detection function, utilising the Canny method [47]. Pixels in identified grain boundary regions were considered not-indexed first and subsequently filled using the MTEX 'fill' function with the half quadratic filter ('halfQuadraticFilter' option). This approach effectively removed spatially independent noise from the orientation measurement data while maintaining sharp gradients at the grain boundaries and sub-structural boundaries. Through this process, the vague grain boundary region generated from the GAN models are eliminated for the following analysis and evaluation.

3.3. Image-based and material-specific evaluation metrics

To verify the quality of the generated microstructural maps, two image-based metrics – Fréchet inception distance (FID) and Peak Signal-to-Noise Ratio (PSNR) – were calculated to quantitively compare the generated and experimental microstructure mappings [48]. Note that Euler angle maps were converted into IPF maps for the image-based evaluation. FID measures the distance between the distributions of generated images and real images in a feature space, typically extracted using a pretrained Inception-v3 neural network. Lower FID scores correspond to a closer resemblance between the two distributions, indicating superior image quality and greater similarity in terms of features and diversity. PSNR is a variation of mean-square error that focuses on pixel-by-pixel comparison. It measures the ratio between the maximum possible power of a signal and the power of corrupting noise that affects the fidelity of its representation. The higher the value of PSNR is, the more acceptable the quality of the generated images. Using these two metrics, both perceptual quality and pixel fidelity of the output images can be evaluated.

It is important to note that the models are not used to generate exact copies of the EBSD images, but rather statistically equivalent representations that carry similar and accurate material information essential for sample characterisation. Therefore, apart from image-based evaluation, materials-related descriptors such as geometry and crystallographic orientation of grains were also considered. They can provide more accurate insights into the model's performance and the characteristics of the generated microstructures. The model's output is a crystal orientation mapping, where each pixel contains three channels corresponding to Euler angle triplets. Grain morphology and grain boundary statistical analyses were performed using the open-source MTEX package in MATLAB. For crystallographic analysis, a 5° misorientation angle was used for the grain calculations in MTEX. The dual approach of employing both image-based and material-specific evaluation metrics ensures a robust assessment of the CycleGANs' capability for high-fidelity surface-to-microstructure mapping.

These evaluations were conducted on a validation dataset that include random surface and microstructure patches for all printing conditions. Additionally, 6 samples with unseen conditions were included for testing. The newly added conditions were within the range of training sample conditions, ensuring a thorough evaluation of model's generalisation capability.

4. Results and discussion

4.1. Quantitative surface profiling and microstructure characterisation

The GAN models aim to bridge the process parameters, surface morphology, and microstructures of printed parts, the correlations of which are investigated through sampling and characterisation. The three process parameters varied in this study collectively contribute to the energy deposited onto the powder bed. This energy density is characterised as volumetric energy density (VED) and is defined by the equation $VED = P/(v \times h \times t)$ [49,50], where P represents power, v represents scan speed, h represents hatch spacing, and t represents layer thickness. The influence of respective VED applied on surface roughness, porosity, and average grain size is presented in Figure 3(a). The surface roughness used here excluded waviness in accordance with ISO 25178 [51] by applying a cut-off wavelength of 0.25 mm, based on prior experience [52–54]. This filtering separated large-scale pattern such as humps from small-scale features like partially melted particles and spatters. The results indicate that variations in porosity and surface roughness exhibit similar trends across the different VED inputs, while changes in average grain size show an inverse relationship. High-quality samples, typically fully dense with a density of 99% or higher and exhibiting low surface roughness, are obtained within a VED range of 120–180 J/mm^3. However, excessive or insufficient energy input can lead to defects that deteriorate mechanical performance. An illustration of the formation mechanism of these defects is shown in Figure 3(c). With insufficient energy input (VED < 120 J/mm^3), the samples typically suffer from lack-of-fusion (LOF) defects. Conversely, excessive energy input (VED > 180 J/mm^3) results in over-fusion. Figure 3(b) shows the classification of all printed sample qualities across the range of printing parameters.

Under LOF condition, there is insufficient thermal energy input to the material. Inadequate laser penetration results in un-melted or partially melted powders, leading to phenomena such as beading up (balling) and LOF pores. This condition produces a rough surface due to Plateau–Rayleigh capillary instabilities in the melt pool [55]. To maintain the uniform capillary pressure inside the pool, the unstable melt pool breaks into discontinuous spherical balls, which serves as the major sources of surface imperfections [3]. The insufficient energy also results in shallow melt pools as indicated by the black dashed lines for sample 1 (Figure 4). The shallow melt pools, with their small radiating surface area in contact with the substrate, cause unidirectional heat dissipation along the melt pool boundary. Consequently, the presence of numerous irregular LOF pores disrupts the epitaxial growth, contributing to small overall grain sizes and random texture in the material [56].

When the energy input is optimal, the melt pool remains stable, leading to a continuous and uniform scan track as shown in the SEM surface image of sample 8 (Figure 4). This stability minimises surface defects and results in a smoother finish. The optimal energy input ensures that powder particles are fully melted and there is sufficient overlap between scan tracks, reducing cavities and porosities [57]. The melt pools penetrate and remelt the previous layers, which favours the epitaxial grain growth along the build direction. With higher laser power and lower scan speed, the resulting shape of the melt pool promotes the formation of textures with a preference for the < 110 > and < 100 > planes [58,59], as evidenced by the presence of more red and green-coloured grains in the IPF maps for sample 8.

On the other hand, excessive energy input for sample 14 ensures that minimal powder particles remain on its surface. However, it induces high vaporisation of the molten material and ejection of metal vapour jet in the form of hot spatters [60]. High laser power and high scan speed can also result in balling. Severe balling on the melt track layer leads to the formation of humping or ripple effects, which are carried forward to subsequent printing layers, seriously impacting the surface quality. Additionally, the larger energy deposition creates deeper and narrow melt pools, which have more contact area with the solid metal below [61]. More heat is conducted downwards, increasing the thermal gradient which is beneficial for epitaxial grain growth [62]. Although this should lead to greater grain coarsening and stronger texture, a slight decrease in the measured average grain size was observed. This trend has also been noted in other studies [40,63], and may be due to the small hatch spacing used for the sample. When hatch spacing is too small, the large melt pool overlaps disrupt square-bottomed columnar grains [64] and increases remelting, leading to smaller grain sizes. The accumulation of local heat at temperature higher than the boiling point also exponentially increases the recoil pressure inside the melt pool [65]. The resultant recoil forces form side dips and cavities, known as keyhole pores, which are spherical in shape [55]. Clusters of fine grain are usually observed at locations near these keyhole pores to a lesser extent than LOF pores.

4.2. Model evaluation

4.2.1. Qualitative analysis

The previous section revealed that the microstructural features of LPBF, particularly porosity and average grain sizes, are associated with surface roughness

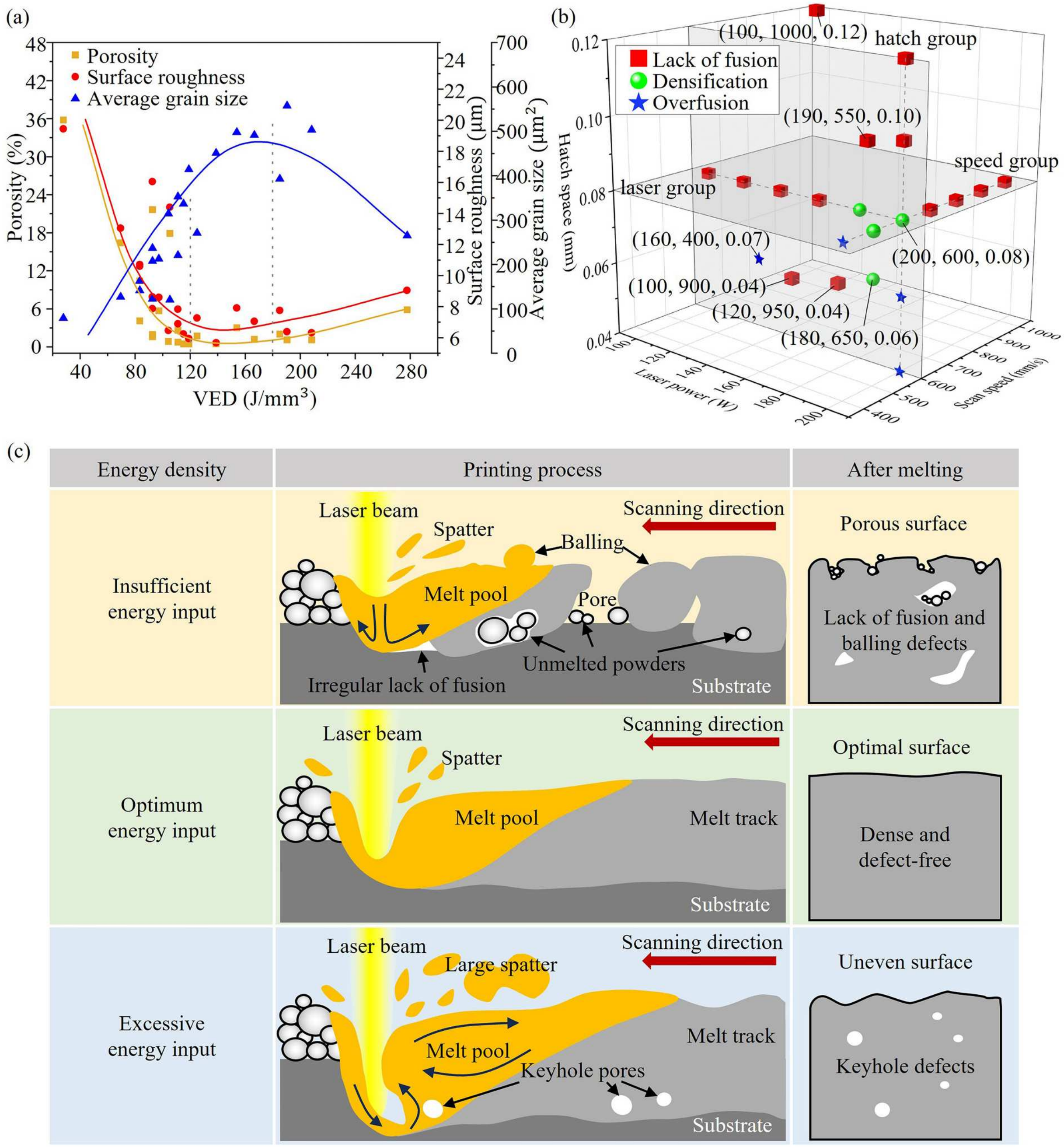

Figure 3. Illustrations of (a) porosity, surface roughness, and average grain size as a function of VED, (b) the sample classification of different parameter groups, and (c) formation mechanisms of the three sample conditions (LOF, densification, and over-fusion).

under various process parameters. To delve deeper into this relationship, a GAN is proposed to establish a connection between as-printed surfaces and their corresponding internal microstructures. Specifically, this study employs a CycleGAN-based model, trained on surface profile data, to examine the PM relationship and to predict internal microstructures.

To evaluate the effectiveness of CycleGAN in learning the relationship between process conditions and corresponding microstructural features, we evaluated the quality of the generated microstructural maps in terms of pixel-level similarity and compare it with CGAN results. Figure 5(a) illustrates the microstructural maps generated by both models alongside the real EBSD IPF maps from the dataset of LPBF-fabricated nickel cube samples. Three samples, with one from each condition class, were selected for visualisation. Based on visual inspection, the microstructures generated by CycleGAN for samples fabricated under varying processing parameters exhibit greater morphological similarity compared to those generated by CGAN, highlighting its adaptability to diverse input conditions. The CycleGAN

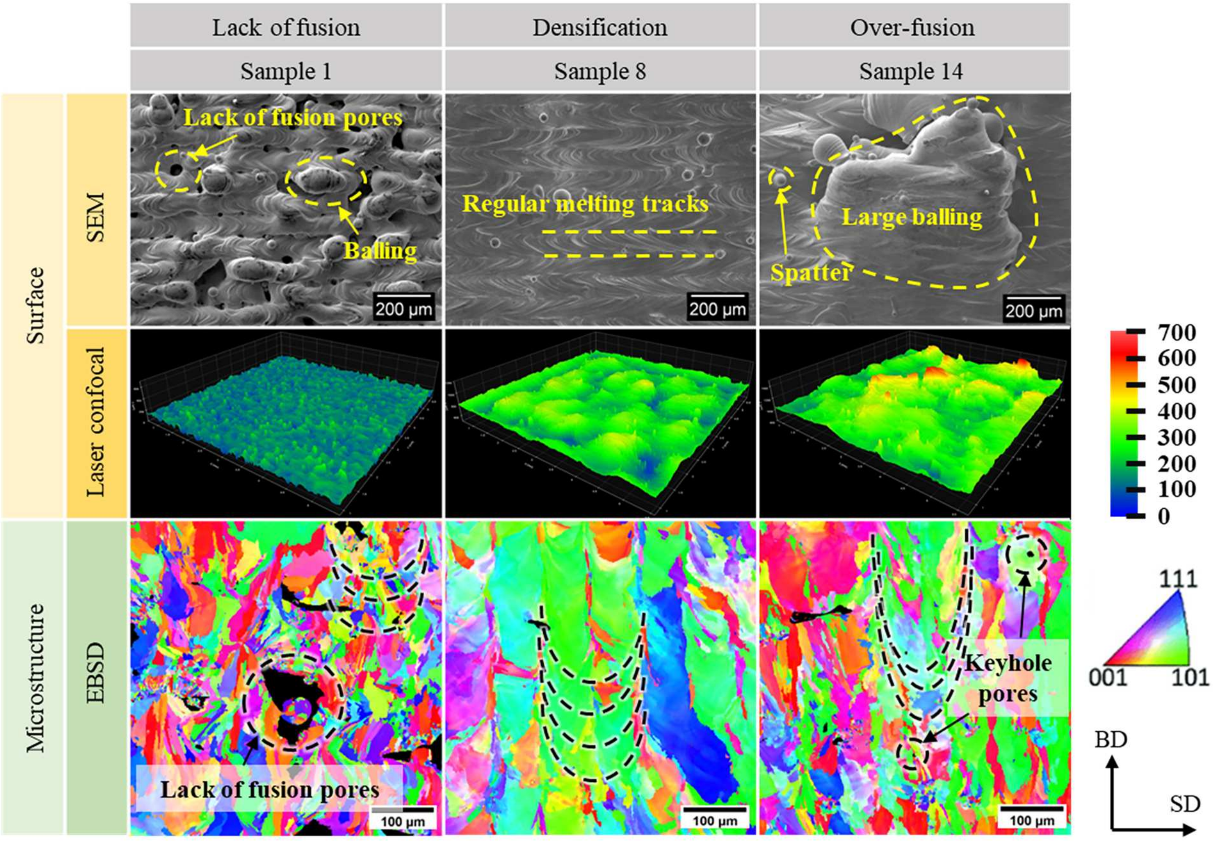

Figure 4. SEM and three-dimensional (3D) laser confocal height maps of top surface morphologies, and EBSD IPF maps of the cross-sectional microstructures of sample 1, 8, and 14.

effectively captured significant attributes such as dimensions, shapes, and colours, which correspond to grain size, boundaries, and orientations of the microstructural representations. For instance, the grains in the real microstructure of sample 8 are relatively larger and exhibit stronger texture compared to those of sample 1. These differences are attributed to higher power density, which promotes adequate melting and epitaxial grain growth. The reconstructed microstructural map accurately replicates these characteristics, notably with large colour blocks representing the larger grains. CycleGAN also showed better performance in synthesising the micrographs with finer features such as small-sized grains and semi-spherical shaped melt pools for some other samples (see Supplementary Figure 2). These features make the generated microstructural maps more comparable to the real EBSD IPF maps. The compelling congruence between the generated and real microstructures underscores CycleGAN's capacity to correctly identify the underlying correlations that link surface characteristics with the intricate nuances of internal microstructures in LPBF manufacturing.

4.2.2. Quantitative analysis

Besides simple visual inspection, the FID and PSNR values were computed to quantify the similarity between ground truth and generated microstructural maps, enabling a direct assessment of the generative models' performance. On the one hand, a higher PSNR in a generated image suggests greater pixel-wise similarity to the ground truth. On the other hand, a lower FID indicates better perceptual image quality [66]. Figure 5(b,c) summarise the FID and PSNR values for both CycleGAN and CGAN, respectively, with the detailed numerical values provided in Supplementary Table 1. From the violin plots, CycleGAN demonstrates an overall lower median FID, higher median PSNR, and similar variance compared to CGAN. This indicates a closer resemblance between the generated and real microstructures, and lower noise content in the CycleGAN outputs. Despite both models producing relatively high FID and low PSNR values, the trend of these quantitative metrics aligns remarkably well with the observations from manual inspection. In view that the microstructural maps are highly complex, and it is difficult to replicate the exact morphology of

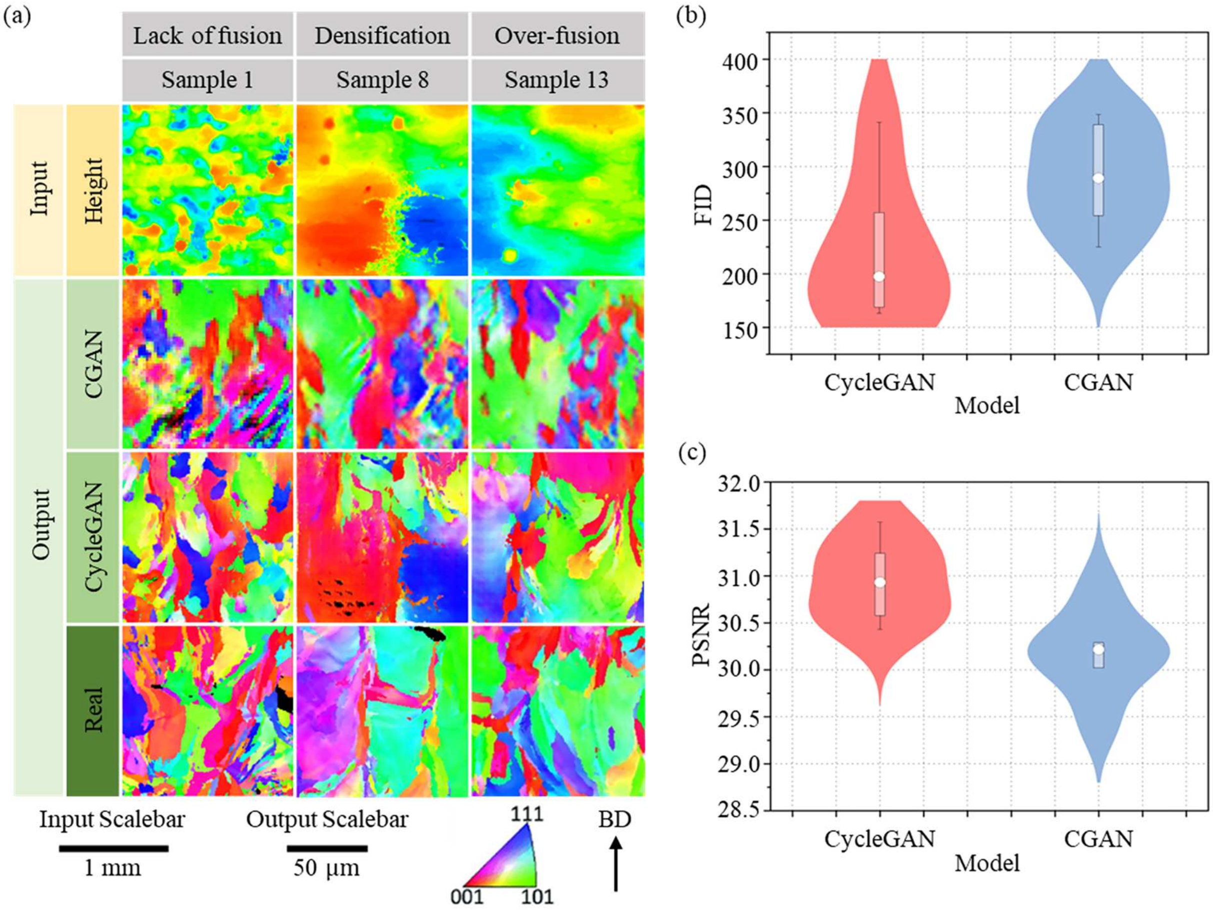

Figure 5. (a) Comparison of real EBSD IPF maps and generated microstructural maps from different GAN models for three samples with one from each condition class, and the violin plots of the (b) FID and (c) PSNR values for all samples.

microstructural features, these two metrics are used for model performance comparison only. The quality of the synthetic images will be assessed based on extracted semantic descriptors of the microstructure, which have physical meaning in this application. Compared to the CGAN benchmark, 87.5% of the samples generated by CycleGAN outperform those by CGAN, as indicated by lower FID and higher PSNR values, except for samples 7 and 8. These two samples, characterised by large grain size and strong texture, received relatively high FID scores. One possible explanation for these inconsistencies is the unbalanced training data, where microstructural maps with large and uniform colour region were underrepresented.

4.2.3. Microstructural characterisation

In addition to directly assessing image quality, it is crucial to ensure that the generated microstructure is statistically representative of the real microstructure. For the additive manufactured parts, the microstructures like grain size, grain shape, texture, and grain boundaries play an important role in determining the mechanical properties and their final performance [67–69]. To assess the morphology distribution, metrics such as grain size, grain shape factor, and grain boundary misorientation angles were selected. The grain shape factor used here is defined as the ratio of grain boundary perimeter over the equivalent perimeter, it primarily assesses how equiaxed or elongated a grain is [70]. The two-sample Kolmogorov – Smirnov (KS) test was used to compare these distributions between generated and ground truth microstructures, and returned a *p*-value which indicates whether there is a significant difference between the distributions. The average *p*-values for 30 randomly selected microstructures which cover 14 of the training samples with different process conditions are shown in Figure 6(a). Most of the values computed are higher than the significance value set at 0.05, particularly for grain size, where only one sample falls below this threshold value. The high *p*-values suggest that the available data do not provide strong evidence of a significant difference between the generated and real microstructure distributions, indicating that the model

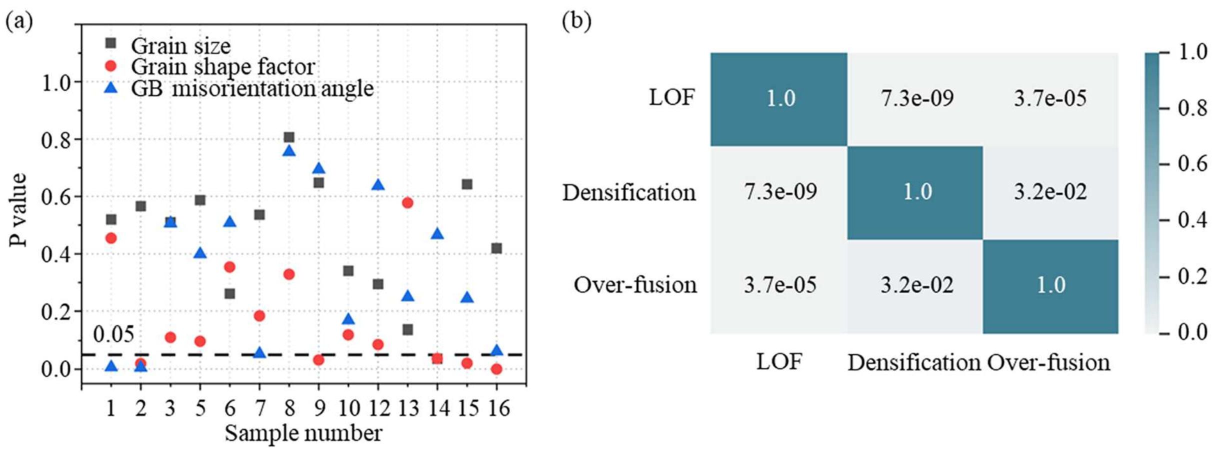

	LOF	Densification	Over-fusion
LOF	1.0	7.3e-09	3.7e-05
Densification	7.3e-09	1.0	3.2e-02
Over-fusion	3.7e-05	3.2e-02	1.0

Figure 6. *P*-values of the two-sample Kolmogorov-Smirnov test computed (a) on the three microstructural descriptors of the ground truth and generated images for random training samples and (b) among different energy input conditions (LOF, densification, and over-fusion).

effectively captures grain size information. In contrast, the *p*-values below the threshold are mainly observed for grain shape factor (5 out of 14) and grain boundary misorientation angle (2 out of 14), highlighting the challenges for the model to learn and generate microstructure map with these correct microstructure features. This difficulty likely arises from their higher dimensional complexity and non-linearity. Noise at the grain boundaries also disproportionately affects the calculation of these features. Considering the significant differences in morphology distributions among different energy input groups, as indicated by the extremely low *p*-values in Figure 6(b), the model demonstrates its ability to capture meaningful distributions related to the process conditions.

To assess the synthesised microstructure's suitability as a statistically equivalent morphological and crystallographic descriptor for LPBF material characterisation in detail, sample 13 was randomly selected and the statistics of its features are depicted in Figure 7. Both the ground truth (Figure 7(a)) and generated (Figure 7(c)) microstructural maps reveal grains growing along the building direction due to the high thermal gradient from the bottom to the top of the melt pool. The generated grains are largely columnar, reflecting the directional solidification typical of high-energy density LPBF processes, and their size closely matches that observed in the actual microstructures. By overlaying histograms of grain size, grain shape factor, and grain boundary misorientation angle from the ground truth and generated microstructural maps (Figure 7(e–g)), a notable agreement is shown in the general distribution of all three features. This observation is consistent with the KS test results for sample 13, where the *p*-values for all three features exceed 0.05. Pole figures in Figure 7(b,d) exhibit considerable similarity between the generated and ground truth microstructural maps. Although there is a noticeable lack of grains with a (101) out-of-plane orientation in the generated microstructural map compared to the ground truth microstructure obtained from EBSD measurements, the strong $< 001 >$//building direction texture still indicates that the model effectively captures the preferred crystallographic orientation. Additionally, when examining the single grains isolated from the maps, as shown in Figure 7(h,i), the colour gradient within individual grain, which denotes variations in orientation, is well-represented in the generated microstructural map. This variation is a common microstructural feature in LPBF due to rapid thermal cycling and complex melt pool dynamics. The kernel average misorientation (KAM) maps of these grains were computed to reveal these subtle changes in orientation within the grains, and they appear visually similar. This indicates that the generated microstructural data can be further processed to determine dislocation density, providing valuable insight into the internal strain and defects [71]. Overall, the close agreement between the synthesised and actual microstructures reflects the high quality and accuracy of the generated microstructural maps, both in general representation and in localised detail.

The material-specific comparisons between the ground truth and generated microstructural maps indicate that a high degree of detail and information density regarding the necessary materials-related features are well replicated and represented in the generated images. The strong alignment suggests that the hidden complex correlations between desired microstructural features and surface features are effectively learned by the selected CycleGAN model.

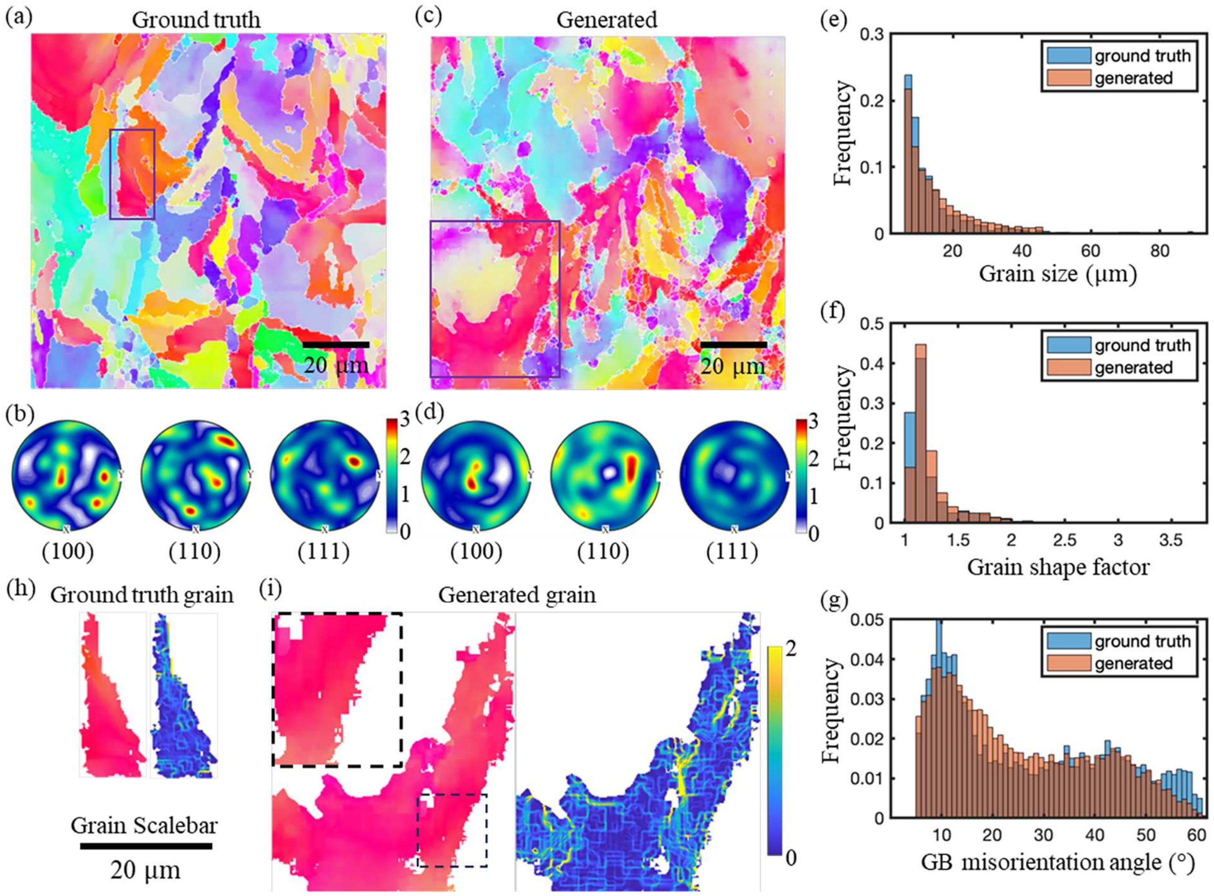

Figure 7. Example IPF maps of (a) ground truth and (c) generated microstructures of a sample, with their respective (b and d) PFs; comparison of distributions for (e) grain size, (f) grain shape factor, and (g) grain boundary misorientation angle between the ground truth and generated microstructures; illustrations of individual grains extracted from (h) ground truth and (i) generated microstructures, and their respective KAM maps.

4.3. Model optimisation and generalisation

4.3.1. CycleGAN input optimisation

The surface of an additively manufactured sample is routinely characterised using a variety of techniques, including OM, SEM, and LSCM. Three types of input images are prepared for the CycleGAN model, all cropped to the same scale to represent the same region of interest on the sample. Figure 8(a) demonstrates an example of generated microstructural map from these three inputs. Visual inspection of the generated microstructural maps reveals that the LSCM surface profiles produce a mapping in which most of the features are preserved. The generated IPF and Euler maps accurately restore essential features from real microstructure, such as grain size, shape, and texture, with fewer unrealistic artifacts such as large black patches, blurred colour edges, or repeated patterns. Between these two types of output, the Euler map outperforms the IPF map by reproducing fine details such as pores and very small grains sometimes observed at the melt pool boundaries. The effectiveness of using surface profiles from LSCM as input was further confirmed by the calculated FID and PSNR values across six randomly selected samples used for evaluation (Figure 8(b,c)). The detailed numerical values of all input-output combinations are provided in Supplementary Table 2. In general, the generated microstructural map in Euler angles from LSCM surface profiles exhibit the lowest FID values and the highest PSNR values compared to all other input-output image combinations. Additionally, the image quality is more consistent across different parameter groups.

Optical images, typically greyscale, serve as a fundamental tool for providing an overall view of the surface texture and for detecting large-scale defects. While OM is limited in its ability to resolve fine details and provide quantitative data, it compensates by offering additional information such as colour variations, which can be instrumental in identifying different phases, contaminants, or oxidation states. The information density of optical images is relatively lower compared to SEM and LSCM. However, their ability to quickly survey

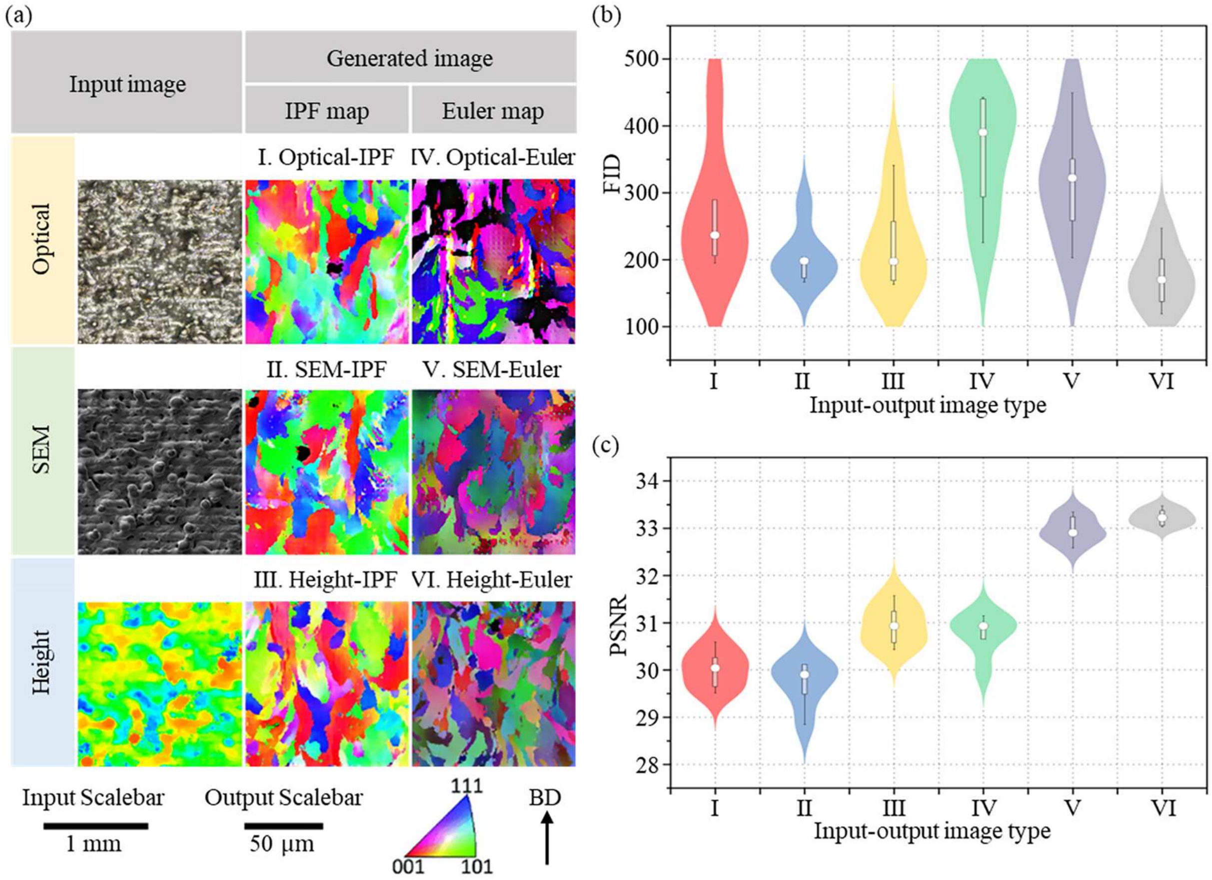

Figure 8. (a) Comparison of generated and ground truth microstructures with different input and output image types for sample 1, and the violin plots of the (b) FID and (c) PSNR values for six randomly selected samples.

large areas makes them valuable for preliminary assessments and for identifying regions of interest for further, more detailed analysis. SEM images are also greyscale but offer significantly higher resolutions than optical images, enabling detailed imaging of surface features with high precision and comprehensive surface characterisation. This makes SEM a common choice for in-depth morphological studies [72]. Although the SEM images were cropped and resized to the same dimension as OM images to match the model's input shape, their high original resolution offer more pixel data to work with, allowing for greater flexibility in resizing without significant quality loss. This high resolution and information density of SEM images, at the same length scale as an OM image, come at the cost of increased time and expense associated with image acquisition. The LSCM bridges the gap between OM and SEM techniques by offering higher resolution than traditional OM in a shorter time than SEM. One of its key advantages lies in generating 3D surface topography maps, which provide enhanced depth of field and streamline the extraction of surface features. The colour scale of LSCM mapping quantitatively correlates with the height of the surface. This additional depth information makes it particularly valuable for applications requiring detailed topographical analysis and 3D reconstructions of surface features. The more detailed structural information of the surface serves as a better indicator of processing conditions of the printed samples, allowing the model to infer potential microstructural feature formation and accurately generate corresponding image patterns.

4.3.2. Microstructure prediction and model generalisation

The generalisation ability of the trained GAN-based model was further tested by generating microstructural features from surface profiles derived from LPBF process parameter combinations that were beyond the scope of the model's training. To verify if the established surface-microstructure relationships can help to predict microstructure distributions in unknown cases, six new process parameter combinations were chosen using a random sampling function code in Python. These combinations had all parameters within the range of trained values and covered all three discussed sample conditions,

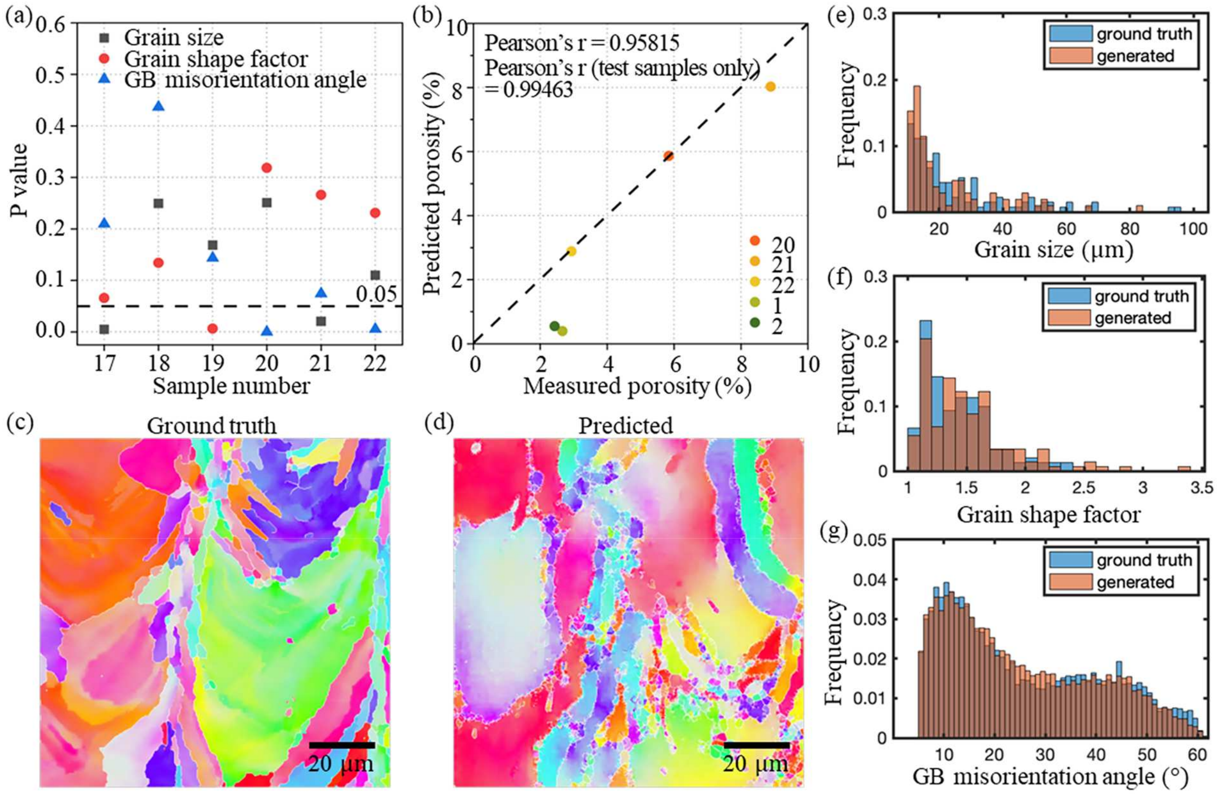

Figure 9. (a) *P*-values of the two-sample Kolmogorov-Smirnov test computed on the three microstructural descriptors of the ground truth and generated microstructural maps for test samples; (b) comparison of predicted porosity and measured porosity of the samples in severe conditions; example IPF maps of (c) ground truth and (d) predicted microstructure of a test sample, and the comparison of distributions for (e) grain size, (f) grain shape factor, and (g) grain boundary misorientation angle between the ground truth and predicted microstructures.

yet they were unseen by the model during training. Samples were printed based on these new parameters, and same characterisation steps were performed to obtain their surface profiles and microstructure, forming the test dataset for assessing accuracy of microstructural features in the predicted maps. Figure 9(a) presents the calculated *p*-values of the two-sample KS test for all testing samples. For the six unseen surface profiles, there is insufficient evidence to support the hypothesis of a significant difference between the real and predicted microstructural maps as most of the *p*-values exceeded the 0.05 threshold. Specifically, only two profiles exhibited notable variations in grain size and grain boundary misorientation angle distributions, while only one profile showed notable variations in grain shape factor distributions, despite the inherent complexity of this feature, as illustrated in Figure 9(a). These findings further confirm the model's ability to learn complex microstructural features and correlations from the collected dataset, and generalise effectively to unseen data.

Figure 9 shows the detailed comparison between the ground truth and predicted microstructural maps of one of the newly printed samples, specifically sample 18. This sample was fabricated with a laser power of 190 W, scan speed of 550 mm/s, and hatch spacing of 0.1 mm. These printing parameters yield a VED value of 115.15 J/mm^3, which is close to the optimal printing condition of 120 J/mm^3. The sufficient energy input results in coarser grains and stronger texture formation, as evidenced by the ground truth IPF map (Figure 9(c)). Similarly, the predicted microstructural map in Figure 9(d) displays some large grains with relatively higher green colour density. Common AM features, such as local grain misorientation and the general alignment of grains with the thermal gradient which explicitly grow towards the centre of the melt pool [55], are also evident. These observations suggest that the model effectively learns both global features (such as texture, grain size, and shape factor) and local features (such as local grain orientation variation, represented by the KAM map). Furthermore, the histograms plotted to quantitatively compare the differences in the distributions of the three main microstructural features (Figure 9(e–g)) demonstrate comparable characteristics. For both ground truth and predicted microstructures, the frequency of grains with size exceeding 40 μm greatly increases, and the general trends in their misorientation angles align more closely compared to those of sample 13. Therefore, this generative model is suitable for predicting microstructural morphology across a wide range of printing conditions.

In addition to the grain morphology, the microstructural defect such as porosity of the samples is also evaluated (Figure 9(b)). Only samples with overall porosity values higher than 10% are considered in this evaluation, as pores in low porosity samples occupy a small percentage area of the image and are difficult for the model to capture. The porosity in the generated images was determined by filtering out black pixels and calculating the porosity percentage using ImageJ [73]. Among all samples, including both training and test samples, five meet this condition. The predicted porosity for all these samples does not differ significantly from the measured porosity, especially for the three test samples. Sample 20, which has an extremely low VED value of 27.78 J/mm^3 and falls outside the training dataset range, still shows a good fit, indicating the superior generalizability of the model. The Pearson correlation coefficient (*r*) for the fitted linear relationship is greater than 95%, and it reaches 99.4% when considering only the test samples. This strong correlation between the predicted and measured porosity highlights the high accuracy in the predicted microstructure. The prediction error mainly comes from samples 1 and 2. This underestimation likely occurs because the model prioritises overall microstructural patterns over porosity. This is an issue when the loss function does not explicitly emphasise small and sparse defect features [74]. These small pores could unintentionally be merged into surrounding grains while performing the pooling process [75], reducing the detected porosity. Additionally, partially filled pores or noise in the generated images may lead to misclassification. The underestimation could be minimised by incorporating a defect-aware loss term to enhance porosity preservation and increase the representation of low-porosity samples in the training dataset through data augmentation techniques.

Despite its high accuracy in capturing critical microstructural features, the CycleGAN model has limitations, particularly in generating sharp edges that correspond to grain boundaries, which are crucial for determining material properties. The model occasionally produces blurred edges and small branches at grain boundaries, which could lead to misinterpretation of grain boundary types and inaccuracies in edge-sensitive property predictions [58]. These challenges underscore the need for further refinement of the CycleGAN model, especially in enhancing its ability to generate more precise and realistic microstructures. Future research may focus on integrating attention-based models to improve the clarity and precision of grain boundaries, reducing the need for post-processing and minimising artifacts.

The use of microstructural image patches for model training, necessitated by computational feasibility concerns, poses challenges in accurately capturing large epitaxial grains that extend beyond individual patches. Consequently, the grain size measured in a single cropped patch may not fully represent the true grain size in the full image. Although the overall trend and correlation between VED and grain size are still preserved at a statistical level, the model's ability to generate microstructures that closely resemble the real samples remains limited. Future improvements should focus on expanding the microstructure dataset and scaling up the CycleGAN model to train on full-sized images by leveraging greater computational resources.

Furthermore, the CycleGAN model could be fine-tuned for application to other LPBF materials, it can also support real-time monitoring of printing quality, as surface profiles can be captured during printing [57] and used to predict evolving microstructures. This capability allows for dynamic adjustments to printing parameters, enabling improved control over the process and enhancing the production efficiency, offering significant potential for process optimisation and quality control in advanced manufacturing.

5 Conclusion

In this study, a novel microstructure characterisation approach using the CycleGAN model was presented, significantly streamlining the traditionally time-consuming process of microstructure analysis. By relying on only surface mappings, the proposed model can generate statistically equivalent microstructure representations, EBSD-like orientation mappings, eliminating the need for cross-sectioning and EBSD measurements. The key conclusion are as follows:

(1) CycleGAN was trained to generate crystal orientation mapping from surface profile input. This CycleGAN model outperforms traditional CGAN models that predict from text-based process parameters with higher PSNR and lower FID values.
(2) The generated microstructure mappings can statistically represent the experimentally measured datasets, as evidenced by the KS test, where most *p*-values exceed 0.05, indicating no significant differences. This demonstrates the model's strong potential to generalise across various LPBF process parameter combinations.

(3) Experimental characterisation confirmed that the surface profile is closely related to the internal microstructure through energy input and thermal history. Particularly, surface roughness has been proved to have correlation with internal average grain size and porosity.

Acknowledgements

The authors would like to thank the personnel at the National Supercomputing Centre (NSCC), Singapore. The computational work for this article was partially performed on resources of the NSCC.

Disclosure statement

No potential conflict of interest was reported by the author(s).

Funding

This study was supported by the Economic Development Board-Singapore and Infineon Technologies Singapore through the Industrial Postgraduate Programme with Nanyang Technological University.

Data availability statement

The data that support the findings of this study are available from the corresponding author upon reasonable request.

ORCID

Kun Zhou http://orcid.org/0000-0001-7660-2911

References

[1] Wang Q, Zhu Z, Guan J, et al. The influence mechanisms of re-fused scanning on the surface roughness, microstructural evolution and mechanical properties of laser powder bed fusion processed AlMgScZr alloy. Opt Laser Technol. 2024;177:111060. doi:10.1016/j.optlastec.2024.111060

[2] Liu Z, Zhao D, Wang P, et al. Additive manufacturing of metals: microstructure evolution and multistage control. J Mater Sci Technol. 2022;100:224–236. doi:10.1016/j.jmst.2021.06.011

[3] DebRoy T, Wei HL, Zuback JS, et al. Additive manufacturing of metallic components–process, structure and properties. Prog Mater Sci. 2018;92:112–224. doi:10.1016/j.pmatsci.2017.10.001

[4] Aboulkhair NT, Simonelli M, Parry L, et al. 3D printing of aluminium alloys: additive manufacturing of aluminium alloys using selective laser melting. Prog Mater Sci. 2019;106:100578. doi:10.1016/j.pmatsci.2019.100578

[5] Gao S, Ji W, Zhu Q, et al. Pulsed-wave laser additive manufacturing of CrCoNi medium-entropy alloys with high strength and ductility. Mater Today. 2024;81:36–46. doi:10.1016/j.mattod.2024.10.004

[6] Wang YM, Voisin T, McKeown JT, et al. Additively manufactured hierarchical stainless steels with high strength and ductility. Nat Mater. 2018;17(1):63–71. doi:10.1038/nmat5021

[7] Zhang T, Huang Z, Yang T, et al. In situ design of advanced titanium alloy with concentration modulations by additive manufacturing. Science. 2021;374(6566):478–482. doi:10.1126/science.abj3770

[8] Gao S, Li Z, Van Petegem S, et al. Additive manufacturing of alloys with programmable microstructure and properties. Nat Commun. 2023;14(1):6752. doi:10.1038/s41467-023-42326-y

[9] Gao S, Hu Z, Duchamp M, et al. Recrystallization-based grain boundary engineering of 316L stainless steel produced via selective laser melting. Acta Mater. 2020;200:366–377. doi:10.1016/j.actamat.2020.09.015

[10] Gokcekaya O, Ishimoto T, Hibino S, et al. Unique crystallographic texture formation in Inconel 718 by laser powder bed fusion and its effect on mechanical anisotropy. Acta Mater. 2021;212:116876. doi:10.1016/j.actamat.2021.116876

[11] Martucci A, Aversa A, Lombardi M. Ongoing challenges of laser-based powder bed fusion processing of Al alloys and potential solutions from the literature—a review. Materials (Basel). 2023;16(3):1084. doi:10.3390/ma16031084

[12] Teferra K, Rowenhorst DJ. Optimizing the cellular automata finite element model for additive manufacturing to simulate large microstructures. Acta Mater. 2021;213:116930. doi:10.1016/j.actamat.2021.116930

[13] Choi JY, Xue T, Liao S, et al. Accelerating phase-field simulation of three-dimensional microstructure evolution in laser powder bed fusion with composable machine learning predictions. Additi Manufact. 2024;79:103938. doi:10.1016/j.addma.2023.103938

[14] Muñiz-Lerma JA, Nommeots-Nomm A, Waters KE, et al. A comprehensive approach to powder feedstock characterization for powder bed fusion additive manufacturing: a case study on AlSi7Mg. Mater (Basel). 2018;11(12):2386. doi:10.3390/ma11122386

[15] Boorani Koopaei F, Javanbakht M, Silani M. A mechanics-based phase-field model and finite element simulations for microstructure evolution during solidification of Ti-6Al-4V. J Mater Eng Perform. 2024;33(15):7552–7563. doi:10.1007/s11665-024-09356-z

[16] Akram J, Chalavadi P, Pal D, et al. Understanding grain evolution in additive manufacturing through modeling. Additi Manufact. 2018;21:255–268. doi:10.1016/j.addma.2018.03.021

[17] Moges T, Ameta G, Witherell P. A review of model inaccuracy and parameter uncertainty in laser powder bed fusion models and simulations. J Manuf Sci Eng. 2019;141(4):040801. doi:10.1115/1.4042789

[18] Cao Z, Liu Q, Liu Q, et al. A machine learning method to quantitatively predict alpha phase morphology in additively manufactured Ti-6Al-4V. NPJ Comput Mater. 2023;9(1):195. doi:10.1038/s41524-023-01152-y

[19] Tang J, Geng X, Li D, et al. Machine learning-based microstructure prediction during laser sintering of alumina. Sci Rep. 2021;11(1):10724. doi:10.1038/s41598-021-89816-x

[20] Durmaz AR, Müller M, Lei B, et al. A deep learning approach for complex microstructure inference. Nat Commun. 2021;12(1):6272. doi:10.1038/s41467-021-26565-5

[21] Jung J, Na J, Park HK, et al. Super-resolving material microstructure image via deep learning for microstructure characterization and mechanical behavior analysis. NPJ Comput Mater. 2021;7(1):96. doi:10.1038/s41524-021-00568-8

[22] Jangid DK, Brodnik NR, Echlin MP, et al. Q-RBSA: high-resolution 3D EBSD map generation using an efficient quaternion transformer network. NPJ Comput Mater. 2024;10(1):27. doi:10.1038/s41524-024-01209-6

[23] Gui Y, Aoyagi K, Bian H, et al. Detection, classification and prediction of internal defects from surface morphology data of metal parts fabricated by powder bed fusion type additive manufacturing using an electron beam. Additi Manufact. 2022;54:102736. doi:10.1016/j.addma.2022.102736

[24] Smoqi Z, Gaikwad A, Bevans B, et al. Monitoring and prediction of porosity in laser powder bed fusion using physics-informed meltpool signatures and machine learning. J Mater Process Technol. 2022;304:117550. doi:10.1016/j.jmatprotec.2022.117550

[25] Yonehara M, Kato C, Ikeshoji T-T, et al. Correlation between surface texture and internal defects in laser powder-bed fusion additive manufacturing. Sci Rep. 2021;11(1):22874. doi:10.1038/s41598-021-02240-z

[26] Gao Z, Ren P, Wang H, et al. Additive manufacture of ultrasoft bioinspired metamaterials. Int J Mach Tools Manuf. 2024;195:104101. doi:10.1016/j.ijmachtools.2023.104101

[27] Gao Z, Zhang X, Wu Y, et al. Damage-programmable design of metamaterials achieving crack-resisting mechanisms seen in nature. Nat Commun. 2024;15(1):7373. doi:10.1038/s41467-024-51757-0

[28] Goodfellow I, Pouget-Abadie J, Mirza M, et al. Generative adversarial networks. Commun ACM. 2020;63(11):139–144. doi:10.1145/3422622

[29] Mirza M, Osindero S. Conditional generative adversarial nets, arXiv preprint arXiv:1411.1784, 2014.

[30] Zhu J-Y, Park T, Isola P, et al. Unpaired image-to-image translation using cycle-consistent adversarial networks. Proc IEEE Inter Conf Comp Vis. 2017; 2242–2251. doi:10.1109/iccv.2017.244

[31] Banko L, Lysogorskiy Y, Grochla D, et al. Predicting structure zone diagrams for thin film synthesis by generative machine learning. Comm Mater. 2020;1(1):15. doi:10.1038/s43246-020-0017-2

[32] Lee JW, Goo NH, Park WB, et al. Virtual microstructure design for steels using generative adversarial networks. Eng Rep. 2021;3(1):e12274. doi:10.1002/eng2.12274

[33] Narikawa R, Fukatsu Y, Wang Z, et al. Generative adversarial networks-based synthetic microstructures for data-driven materials design. Adv Theory Simul. 2022;5(5):2100470. doi:10.1002/adts.202100470

[34] Khan A, Lee C-H, Huang PY, et al. Leveraging generative adversarial networks to create realistic scanning transmission electron microscopy images. NPJ Comput Mater. 2023;9(1):85. doi:10.1038/s41524-023-01042-3

[35] Hess P, Drüke M, Petri S, et al. Physically constrained generative adversarial networks for improving precipitation fields from Earth system models. Nat Mach Intell. 2022;4(10):828–839. doi:10.1038/s42256-022-00540-1

[36] Ma B, Wei X, Liu C, et al. Data augmentation in microscopic images for material data mining. NPJ Computational Materials. 2020;6(1):125. doi:10.1038/s41524-020-00392-6

[37] Hu H, Pang X, Li Y, et al. A comparison study of high purity nickel fabricated by laser powder bed fusion and subjected to dynamic plastic deformation. Materialia. 2024;33:102044. doi:10.1016/j.mtla.2024.102044

[38] Wilkinson AJ, Britton TB. Strains, planes, and EBSD in materials science. Mater Today. 2012;15(9):366–376. doi:10.1016/S1369-7021(12)70163-3

[39] Britton TB, Jiang J, Guo Y, et al. Tutorial: crystal orientations and EBSD—or which way is up? Mater Charact. 2016;117:113–126. doi:10.1016/j.matchar.2016.04.008

[40] Yue T, Zou Z, Zhang S, et al. Influence of volumetric energy density on the tribological behaviors of pure nickel fabricated by laser powder bed fusion. Virtual Phys Prototyp. 2023;18(1):e2262449. doi:10.1080/17452759.2023.2262449

[41] Metelkova J, Vanmunster L, Haitjema H, et al. Texture of inclined up-facing surfaces in laser powder bed fusion of metals. Additi Manufact. 2021;42:101970. doi:10.1016/j.addma.2021.101970

[42] Zhou J, Han X, Li H, et al. Investigation of layer-by-layer laser remelting to improve surface quality, microstructure, and mechanical properties of laser powder bed fused AlSi10Mg alloy. Mater Des. 2021;210:110092. doi:10.1016/j.matdes.2021.110092

[43] Anantatamukala A, Krishna KM, Dahotre NB. Generative adversarial networks assisted machine learning based automated quantification of grain size from scanning electron microscope back scatter images. Mater Charact. 2023;206:113396. doi:10.1016/j.matchar.2023.113396

[44] Zargari A, Topacio BR, Mashhadi N, et al. Enhanced cell segmentation with limited training datasets using cycle generative adversarial networks. Iscience. 2024;27(5):109740. doi:10.1016/j.isci.2024.109740

[45] Isola P, Zhu J-Y, Zhou T, et al. Image-to-image translation with conditional adversarial networks. Proc IEEE Conf Comput Vis Pattern Recog. 2017: 5967–5976. doi:10.1109/cvpr.2017.632

[46] Bachmann F, Hielscher R, Schaeben H. Grain detection from 2d and 3d EBSD data—specification of the MTEX algorithm. Ultramicroscopy. 2011;111(12):1720–1733. doi:10.1016/j.ultramic.2011.08.002

[47] Canny J. A computational approach to edge detection. IEEE Trans Pattern Anal Mach Intell. 1986;6:679–698. doi:10.1109/TPAMI.1986.4767851

[48] Sara U, Akter M, Uddin MS. Image quality assessment through FSIM, SSIM, MSE and PSNR—a comparative study. J Comput Comm. 2019;7(3):8–18. doi:10.4236/jcc.2019.73002

[49] Guan J, Wang Q. Laser powder bed fusion of dissimilar metal materials: a review. Mater (Basel). 2023;16(7):2757. doi:10.3390/ma16072757

[50] Meier H, Haberland C. Experimental studies on selective laser melting of metallic parts. Materialwiss Werkstofftech. 2008;39(9):665–670. doi:10.1002/mawe.200800327

[51] Iso E. 4287–geometrical product specifications (GPS)–surface texture: profile method–terms, definitions and

surface texture parameters. International Organization for Standardization: Geneva, Switzerland, 1997.

[52] Newton L, Senin N, Chatzivagiannis E, et al. Feature-based characterisation of Ti6Al4V electron beam powder bed fusion surfaces fabricated at different surface orientations. Additi Manufact. 2020;35:101273. doi:10.1016/j.addma.2020.101273

[53] Charles A, Elkaseer A, Paggi U, et al. Down-facing surfaces in laser powder bed fusion of Ti6Al4V: Effect of dross formation on dimensional accuracy and surface texture. Additi Manufact. 2021;46:102148. doi:10.1016/j.addma.2021.102148

[54] Diaz A. Surface texture characterization and optimization of metal additive manufacturing-produced components for aerospace applications. In: Froes F, Boyer R, editors. *Additive manufacturing for the aerospace industry*. Elsevier; 2019. p. 341–374. doi:10.1016/b978-0-12-814062-8.00018-2

[55] Wang J, Zhu R, Liu Y, et al. Understanding melt pool characteristics in laser powder bed fusion: An overview of single-and multi-track melt pools for process optimization. Adv Powder Mater. 2023;2(4):100137. doi:10.1016/j.apmate.2023.100137

[56] Nabavi SF, Dalir H, Farshidianfar A. A comprehensive review of recent advances in laser powder bed fusion characteristics modeling: metallurgical and defects. Inter J Adv Manufact Technol. 2024;132(5):2233–2269. doi:10.1007/s00170-024-13491-1

[57] Agrawal AK, Thoma DJ. High-throughput surface characterization to identify porosity defects in additively manufactured 316L stainless steel. Additi Manufact Lett. 2022;3:100093. doi:10.1016/j.addlet.2022.100093

[58] Sofinowski KA, Raman S, Wang X, et al. Layer-wise engineering of grain orientation (LEGO) in laser powder bed fusion of stainless steel 316L. Additi Manufact. 2021;38:101809. doi:10.1016/j.addma.2020.101809

[59] Sun S-H, Ishimoto T, Hagihara K, et al. Excellent mechanical and corrosion properties of austenitic stainless steel with a unique crystallographic lamellar microstructure via selective laser melting. Scr Mater. 2019;159:89–93. doi:10.1016/j.scriptamat.2018.09.017

[60] Narasimharaju SR, Zeng W, See TL, et al. A comprehensive review on laser powder bed fusion of steels: Processing, microstructure, defects and control methods, mechanical properties, current challenges and future trends. J Manuf Process. 2022;75:375–414. doi:10.1016/j.jmapro.2021.12.033

[61] Fan H, Shi Q, Wang C, et al. Laser powder bed fusion of bimetallic stainless steel/nickel-based superalloy: interface and mechanical properties. Mater Sci Eng A. 2023;877:145193. doi:10.1016/j.msea.2023.145193

[62] Li J, Qu H, Bai J. Grain boundary engineering during the laser powder bed fusion of TiC/316L stainless steel composites: new mechanism for forming TiC-induced special grain boundaries. Acta Mater. 2022;226:117605. doi:10.1016/j.actamat.2021.117605

[63] Cruz MLD, Yakubov V, Li X, et al. Microstructure evolution in laser powder bed fusion-built Fe-Mn-Si shape memory alloy. Microstructures. 2023;3.

[64] Hu Z, Gao S, Tai J, et al. Columnar grain width control for SS316L via hatch spacing manipulation in laser powder bed fusion. Mater Res Lett. 2023;11(3):231–238. doi:10.1080/21663831.2022.2140018

[65] Guo L, Wang H, Liu H, et al. Understanding keyhole induced-porosities in laser powder bed fusion of aluminum and elimination strategy. Int J Mach Tools Manuf. 2023;184:103977. doi:10.1016/j.ijmachtools.2022.103977

[66] Ren X, Hui Q, Zhao X, et al. BESRGAN: boundary equilibrium face super-resolution generative adversarial networks. IET Image Proc. 2023;17(6):1784–1796. doi:10.1049/ipr2.12755

[67] Zhao L, Song L, Santos Macías JG, et al. Review on the correlation between microstructure and mechanical performance for laser powder bed fusion AlSi10Mg. Additi Manufact. 2022;56:102914. doi:10.1016/j.addma.2022.102914

[68] Van Cauwenbergh P, Samaee V, Thijs L, et al. Unravelling the multi-scale structure–property relationship of laser powder bed fusion processed and heat-treated AlSi10Mg. Sci Rep. 2021;11(1):6423. doi:10.1038/s41598-021-85047-2

[69] Fu J, Qu S, Ding J, et al. Comparison of the microstructure, mechanical properties and distortion of stainless steel 316 L fabricated by micro and conventional laser powder bed fusion. Additi Manufact. 2021;44:102067. doi:10.1016/j.addma.2021.102067

[70] Xu J, Brodin H, Peng RL, et al. Effect of heat treatment temperature on the microstructural evolution of CM247LC superalloy by laser powder bed fusion. Mater Charact. 2022;185:111742. doi:10.1016/j.matchar.2022.111742

[71] Sun S, Tian Y, Lin H, et al. Revisiting the role of prestrain history in the mechanical properties of ultrafine-grained CoCrFeMnNi high-entropy alloy. Mater Sci Eng A. 2021;801:140398. doi:10.1016/j.msea.2020.140398

[72] Ahamed H, Kumar VS. A comparative study on the milling speed for the synthesis of nano-structured Al 6063 alloy powder by mechanical alloying. J Miner Mater Charact Eng. 2011;10(6):507–515. doi:10.4236/jmmce.2011.106038

[73] Rueden CT, Schindelin J, Hiner MC, et al. ImageJ2: ImageJ for the next generation of scientific image data. BMC Bioinformat. 2017;18:1–26. doi:10.1186/s12859-017-1934-z

[74] Zhang J, Sun S, Song W, et al. A novel convolutional neural network for enhancing the continuity of pavement crack detection. Sci Rep. 2024;14(1):1–20. doi:10.1038/s41598-023-50600-8

[75] Saeed F, Ahmed M, Gul M, et al. A robust approach for industrial small-object detection using an improved faster regional convolutional neural network. Sci Rep. 2021;11(1):23390. doi:10.1038/s41598-021-02805-y